Energy & Environmental Science

ROYAL SOCIETY OF CHEMISTRY

PAPER

View Article Online
View Journal



Cite this: DOI: 10.1039/d5ee05206h

# A π-interactive additive unlocks enhanced zinc anode rechargeability: unveiling the critical role of adsorption layer dynamics

Yuan Shang,[a] Yingna Ding,†[a] Ravindra Kokate,†[a] Ashutosh Rana,[b] Jeffrey E. Dick,[bc] Xinyuan Wu,[d] Bram Hoex,[d] Mingyue Wang,[e] Nana Wang,[f] Qihui Zhang,[a] Priyank Kumar*[a] and Dipan Kundu*[a]

Received 3rd September 2025,
Accepted 27th October 2025

DOI: 10.1039/d5ee05206h

rsc.li/ees

Aqueous zinc-ion batteries are promising for a safe, inexpensive, and sustainable platform for stationary energy storage, but their reversibility remains limited by dendrite and corrosion-mediated failure of the zinc anode. While low-concentration electrolyte additives have emerged as scalable solutions, the mechanistic underpinnings of their interfacial dynamics that dictate whether they enable long-term rechargeability or trigger premature dendritic failure remain poorly understood. Here, we investigate a series of π-interactive aromatic alcohols and a cycloaliphatic reference additive and uncover how additive–zinc and additive–additive interactions jointly govern the formation, spatial organization, packing density, and mobility of the additive film. These interfacial dynamics govern $Zn^{2+}$ transport, corrosion suppression, and zinc deposition morphology. Phenol, which strikes a balance between adsorption strength and interfacial mobility, forms a thick yet dynamic layer that suppresses hydrogen evolution mediated corrosion while promoting uniform zinc deposition. This leads to excellent cycling stability with nearly 2 Ah $cm^{-2}$ cumulative plated capacity in a practically relevant asymmetric configuration at 24% depth of discharge under demanding 4 mA $cm^{-2}$–4 mAh $cm^{-2}$, including a thin separator and low electrolyte-to-capacity ratio, with the coulombic efficiency reaching 99.89% under kinetic control compared to 95.94% for the additive-free electrolyte. Full cell and pouch-cell tests further validate phenol's efficacy, establishing adsorption layer dynamics as a new paradigm for rationalizing electrolyte additives' efficacy in regulating zinc anode reversibility in aqueous batteries.

## Broader context

The global push toward decarbonized energy systems has intensified the need for safe, affordable, and scalable stationary energy storage. Aqueous zinc-ion batteries (AZIBs) offer intrinsic safety, low cost, and environmental compatibility, but their practical deployment is hindered by poor zinc anode rechargeability due to dendritic growth and corrosion. Electrolyte additives provide a scalable solution, yet their development has largely relied on empirical screening with limited mechanistic understanding. This study introduces a high-performing π-interactive additive that significantly enhances zinc anode rechargeability under demanding conditions. Beyond performance gains, the study establishes a mechanistic framework based on adsorption layer dynamics, revealing how additive–zinc and additive–additive interactions govern the interfacial additive film structure, which in turn dictates zinc deposition characteristics and corrosion suppression. The findings challenge the widely implied assumption that stronger adsorption is inherently beneficial, showing instead that dynamic interfacial behavior, arising from a balance between surface affinity and intermolecular forces, is critical for enhanced zinc reversibility. By decoupling additive efficacy from static descriptors and validating the approach across cell configurations under practically relevant conditions, this study provides a more robust basis for rational additive design aimed at improving zinc metal anode rechargeability in AZIBs.

[a] LBRI, School of Chemical Engineering, UNSW Sydney, Kensington, NSW, 2052, Australia. E-mail: priyank.kumar@unsw.edu.au, d.kundu@unsw.edu.au
[b] Department of Chemistry, Purdue University, West Lafayette, IN, 47907, USA
[c] Elmore Family School of Electrical and Computer Engineering, Purdue University, West Lafayette, IN, 47907, USA
[d] School of Photovoltaic and Renewable Energy Engineering, UNSW Sydney, Kensington, NSW, 2052, Australia
[e] Institute for Superconducting and Electronic Materials, Faculty of Engineering and Information Sciences, University of Wollongong, North Wollongong, NSW, 2500, Australia
[f] Centre for Clean Energy Technology, School of Mathematical and Physical Sciences, Faculty of Science, University of Technology Sydney, Sydney, NSW, 2007, Australia
† Equal contributions.

## Introduction

The variability inherent in renewable energy generation necessitates the development of robust cost-effective stationary energy storage technologies. In this regard, aqueous batteries have emerged as promising alternatives to conventional lithium-ion batteries, due to their potential for offering competitive energy densities with superior safety and lower costs.[1,2] Among them, aqueous Zn-ion batteries (AZIBs) stand out, thanks to zinc's abundance, favorable redox potential to reversibly operate with an aqueous electrolyte (−0.76 V *vs.* the standard hydrogen electrode), and high theoretical capacity (820 mAh $g^{-1}$).[3] However, issues related to the repeated electrochemical cycling of zinc metal pose significant reversibility and long-term cycling stability challenges, hindering the practical development of AZIBs.[4,5] This instability is not only influenced by zinc deposition current density and deposition capacity (depth of discharge) but is also exacerbated by parasitic side reactions at zinc inherent in aqueous electrolytes.[6,7] Dendrite formation, a major contributor to limited rechargeability, arises from uncontrolled Zn nucleation and growth, driven by surface heterogeneity and localized current hotspots.[8] Concurrently, the aqueous electrolyte promotes self-corrosion and hydrogen evolution at the Zn anode, consuming protons, depleting active zinc, and increasing local pH.[9] These reactions lead to the formation of insulating byproducts such as zinc hydroxide sulfate ($Zn_4SO_4(OH)_6{\cdot}xH_2O$, ZSH), which obscure active sites and further disrupt uniform Zn plating. Over time, ZSH accumulation impedes charge transfer, increases voltage polarization, and degrades zinc reserve by electrically isolating active zinc.[10] Additionally, corrosion persists even during idle periods, accelerating Zn loss and undermining long-term stability, especially problematic when using thin Zn electrodes to achieve low N/P ratios for higher energy density.[10,11]

To mitigate chemical and electrochemical zinc corrosion and dendritic growth, various electrolyte engineering strategies[12–14] have been developed that suppress water activity and regulate Zn deposition. One common approach involves increasing the salt concentration in the electrolyte to reduce water reactivity at the Zn interface.[15] However, the associated high cost, viscosity, and sluggish ion transport will likely limit its practical viability. Alternatively, tailoring the anion interfacial chemistry to form a protective solid–electrolyte interphase (SEI) on zinc can shield it from direct electrolyte contact.[16–19] While this improves cycling stability and Zn plating uniformity, maintaining a robust SEI over extended operation, especially with significant volume fluctuations of zinc, will be challenging. Organic additives with a strong affinity for Zn have shown promise by preferentially adsorbing onto the Zn surface, modulating the interfacial electric field, and promoting uniform deposition.[20–22] Our earlier work identified adsorption energy, solvation energy, and association energy as key descriptors governing organic additive performance, with adsorption energy emerging as the most influential predictor of additive efficacy, followed by the solvation energy, based on machine learning analysis.[23] This prompted us to explore aromatic alcohols whose π–metal interactions and low $pK_a$ hydroxyl groups can result in strong but varied adsorption behavior. The aim of investigating these aromatic compounds was to understand whether their distinct adsorption energetics and characteristics can reveal deeper insights into the mechanistic underpinnings of organic additive performance in addressing zinc anode's reversibility concerns. Is strong adsorption alone sufficient to ensure zinc rechargeability, or are structure, thickness, and reversibility of the adsorbed film also critical? What governs interfacial additive layer properties, and what are the required properties to balance $Zn^{2+}$ transport and zinc corrosion suppression? Can these mechanistic insights guide the design of a high-performing additive that transcends conventional descriptors?

To this end, we selected phenol and a few of its derivatives and a cycloaliphatic reference, cyclohexanol, as electrolyte additives. In-depth computational and a suite of advanced experimental analyses, including, for the first time in the context of electrolyte additive design, adsorption isotherm analysis, we uncover how additive–zinc and additive–additive interactions jointly govern the formation, spatial organization, packing density, and dynamic behavior of the additive film, which in turn dictate $Zn^{2+}$ transport, corrosion suppression, and zinc deposition morphology. By systematically correlating these interfacial dynamics with electrochemical metrics such as overpotential, charge transfer resistance, and long-term cycling stability across symmetric, asymmetric, full-cell, and pouch-cell formats under demanding testing conditions, we demonstrate that phenol achieves a unique balance: it forms a thick yet mobile interfacial layer that enables uniform zinc deposition while effectively mitigating water-induced corrosion. This study establishes a mechanistic framework for additive exploration, where adsorption dynamics, rather than static adsorption strength alone, emerge as a critical determinant of zinc anode reversibility.

## Results and discussion

### Adsorption characteristics and their correlation with zinc cycling

The refined adsorption and solvation energy values of phenol derivatives and cyclohexanol are summarized in Table S1. Adsorption energies were computed for both the head (interacting *via* the –OH group – head on) and planar (the aromatic π-ring parallel to the zinc surface) interaction configurations for these additives, as shown in Fig. 1a and b, respectively. The results highlight that the flat interaction (Fig. 1b), driven predominantly by van der Waals forces, leads to notably higher adsorption energies for the aromatic molecules with delocalized π-system than the cycloaliphatic cyclohexanol. This emphasizes the critical role of molecular geometry and the presence of a π-electron cloud in influencing the adsorption behaviour of additives through enhanced interfacial interactions.

Bader charge analysis and charge density difference (CDD) calculations were performed for both head-on and planar

 

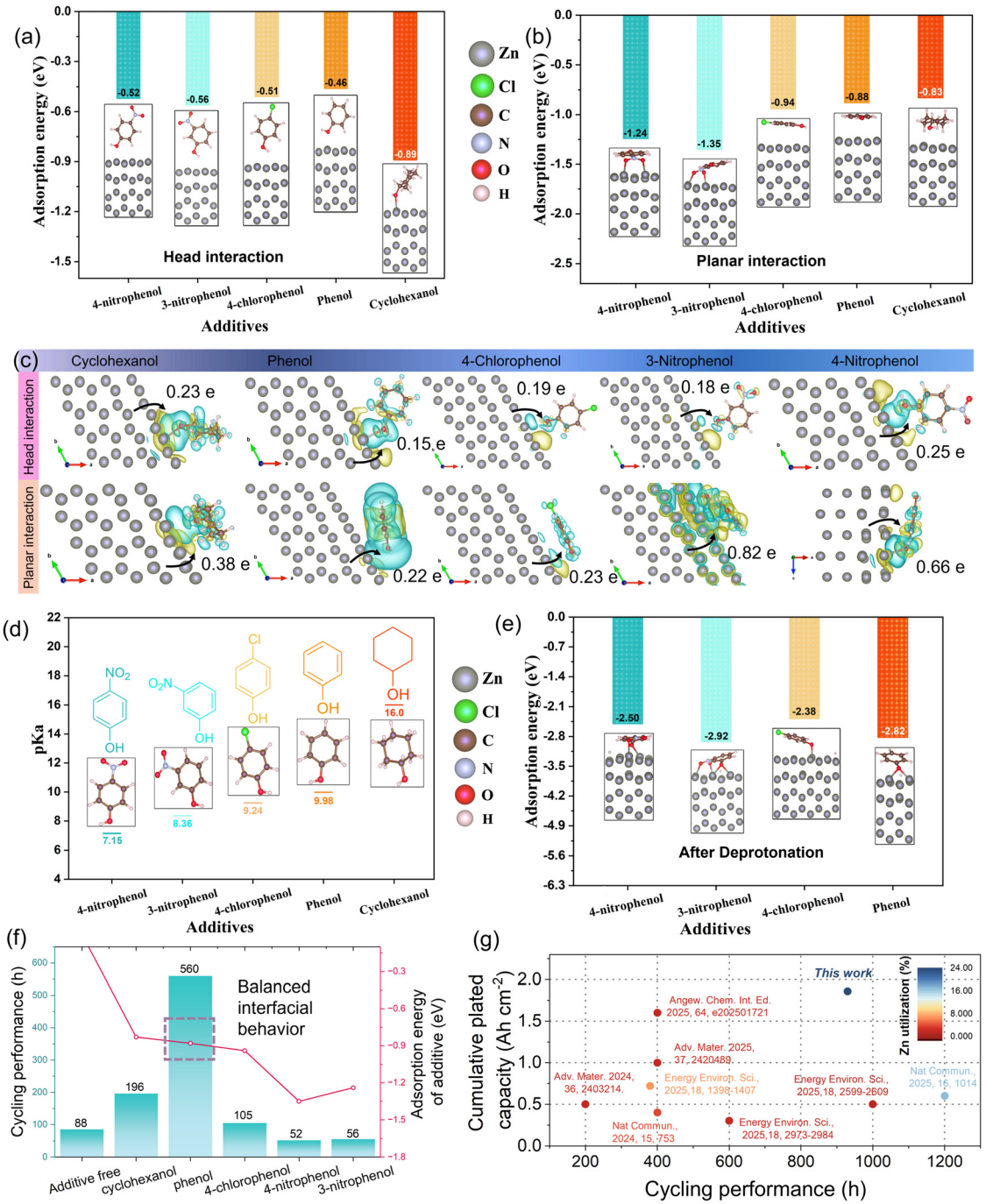


Fig. 1 Computational investigation of additive adsorption characteristics and energetics, and its correlation with zinc cycling. Adsorption energies of the additives for (a) head-on and (b) planar interaction configurations. (c) Charge density difference (CDD) maps upon adsorption, where yellow and cyan regions indicate charge loss and gain, respectively. (d) Molecular structures of the additives annotated with their corresponding p$K_a$ values. (e) Adsorption energies of the additives following hydrogen dissociation. (f) The comparison of cycling performance obtained at 4 mA cm$^{-2}$ and 4 mAh cm$^{-2}$ (20 μm Zn, 34%DoD) and calculated adsorption energy for different additives. (g) The cumulative plated capacity, cycling performance (hours) and Zn utilization in our Zn–Ti asymmetric configuration compared with other reported Zn–Ti[24,25] or Zn–Cu cells.[26–30]

configurations to further elucidate the interfacial interactions. As shown in Fig. 1c, the CDD plots and corresponding Bader values confirm a consistent electron transfer from the Zn surface to the additive molecules, indicating that Zn acts as an electron donor and the additives as electron acceptors. Notably, the planar configurations exhibit higher charge transfer than the head-on cases, particularly for the phenol derivatives, consistent with their stronger adsorption energies. For example, in the case of phenol, the charge transfer increases from 0.15|$e$| (head-on) to 0.22|$e$| (planar), highlighting

enhanced interfacial interactions. The CDD plots further support this observation, showing yellow lobes (electron depletion) on the Zn surface and cyan regions (electron accumulation) on the additive molecules, clearly illustrating the donor–acceptor interaction pattern.

Interestingly, these organic molecules exhibit varying tendencies for hydrogen dissociation, with p$K_a$ values ranging from 7.15 to 16 (Fig. 1d). Since deprotonation produces a negatively charged $O^-$ group, it influences the O–H bond length and, consequently, the molecule's adsorption energy on the zinc surface. This relationship was probed both experimentally and computationally. A computational model with 10 water molecules surrounding the additive molecule, which mimics the additive–water interactions (Fig. S1a), was used to calculate O–H bond lengths as indicators of dissociation in the presence of water and compared to the O–H bond lengths in the case with no water molecules. These computations showed pronounced O–H bond length elongation in the presence of water, thus capturing the O–H dissociation behavior. A polynomial regression analysis (Fig. S1b) of O–H bond length changes (Table S2) against p$K_a$ values yielded a strong correlation ($R^2$ = 0.84), confirming that lower p$K_a$ values correspond to greater bond length elongations and stronger deprotonation effects. The extent of hydrogen dissociation was also experimentally assessed by measuring pH changes after dissolving 50 mM of each additive in 1 M $ZnSO_4$ electrolyte (Fig. S2). As expected, additives with lower p$K_a$ values cause a greater drop in pH, indicating higher dissociation.

To quantify how O–H dissociation affects interactions with the zinc surface, adsorption energies were calculated for the dissociated forms and compared to the non-dissociated ones (Table S3). Cyclohexanol, with negligible dissociation (p$K_a$ = 16.0), was excluded from the dissociated state analysis. As shown in Fig. 1e, all dissociated molecules exhibit stronger adsorption on the zinc surface compared to their neutral forms (Table S3); for example, the adsorption energy of 4-nitrophenol, which shows the lowest p$K_a$ value (and thus the highest tendency to get deprotonated), increased from −1.24 eV to −2.50 eV upon deprotonation. Considering both p$K_a$ values and adsorption energies, cyclohexanol (p$K_a$ 16) and phenol (p$K_a$ 10) tend to retain their molecular forms, resulting in moderate adsorption. In contrast, additives such as 4-chlorophenol, 3-nitrophenol, and 4-nitrophenol (all with p$K_a$ values below 10) are more prone to O–H bond dissociation, leading to stronger adsorption.

To assess the impact of varying effective adsorption energetics on the Zn anode cycling, the different additives were introduced into 1 M $ZnSO_4$ at a 50 mM concentration. Cells were cycled (Fig. S3 and S4) in a Zn–Ti asymmetric configuration, which provides an accurate assessment of the zinc rechargeability,[10] with a limited Zn anode (20 μm) and electrolyte volume (50 μL or 12.5 μL $mAh^{-1}$ E/C ratio), under a demanding 4 mA–4 mAh $cm^{-2}$, corresponding to 34% Zn depth of discharge (DoD), which allows a relatively quick screening of the impact of different additives. The 50 mM concentration was chosen for the feasibility of achieving this concentration across additives and its effectiveness in enhancing Zn rechargeability (Fig. S5). Zinc cyclability screening data, along with the additives' adsorption energies presented in Fig. 1f, identify phenol as the most effective additive, enabling over 560 hours of stable cycling at a high 34% depth of discharge (DoD). In contrast, other additives with either weaker or overly strong adsorption characteristics result in significantly shorter lifespans. Strongly adsorptive 4-chlorophenol, 3-nitrophenol, and 4-nitrophenol suffer rather early failures by short circuit, suggesting that very strong adsorption has a negative impact on the zinc rechargeability. Notably, phenol exhibits superior performance, even under a demanding 24% depth of discharge (DoD), outperforming recent literature-reported additives tested under milder conditions, including lower DoDs in asymmetric configuration (Fig. 1g). Interestingly, except for the phenol-containing electrolyte, which fails due to cell polarization from zinc depletion, all others tend to fail *via* dendrite-induced short circuits. It can be said that phenol effectively suppresses the zinc deposition instability, eliminating dendritic failure. These findings suggest that zinc rechargeability is governed not only by adsorption strength, *i.e.*, additive–zinc interactions, but also by π–π and other intermolecular van der Waals forces between additive molecules at the zinc interface, which shape the spatial and temporal characteristics of the adsorbed layer. These dynamics can decisively steer the system toward either long-term rechargeability or premature failure through dendritic growth.

### Adsorption layer dynamics governing zinc nucleation and growth

Further insights into the thermodynamics of zinc–additive interactions were obtained through adsorption isotherm analysis, which allowed for the determination of the adsorption constant ($K_{ads}$) and the corresponding Gibbs free energy of adsorption ($\Delta G^{\circ}_{ads}$). Fitting the extent of the additive surface coverage $\theta$ on the zinc metal surface as a function of the additive concentration in the electrolyte to different isotherm models also provided valuable information on the nature of the dynamic adsorption layer and additive–additive interactions, amongst others. Complete details of this analysis are provided in the SI. When plotted on a ln–ln scale as $\theta$ *versus* additive concentration (Somasundaran–Fuerstenau isotherm), the isotherm (Fig. 2a) can be divided into four distinct regions, each reflecting characteristic interfacial behavior and concentration regimes. In region I, adsorption follows Henry's law, where monomeric adsorption occurs *via* electrostatic attraction at low surface coverage. Region II begins at a critical hemimicelle concentration (HMC), where a sharp increase in adsorption arises from lateral interactions among additive molecules, leading to hemimicellar aggregate formation. As the surface charge becomes neutralized, region III emerges, characterized by a reduced adsorption slope and continued lateral interactions. Finally, region IV corresponds to the saturation plateau beyond the critical micelle concentration (CMC), where micelle formation and hydrophobic interactions dominate, limiting further adsorption. Given the surface heterogeneity of Zn and

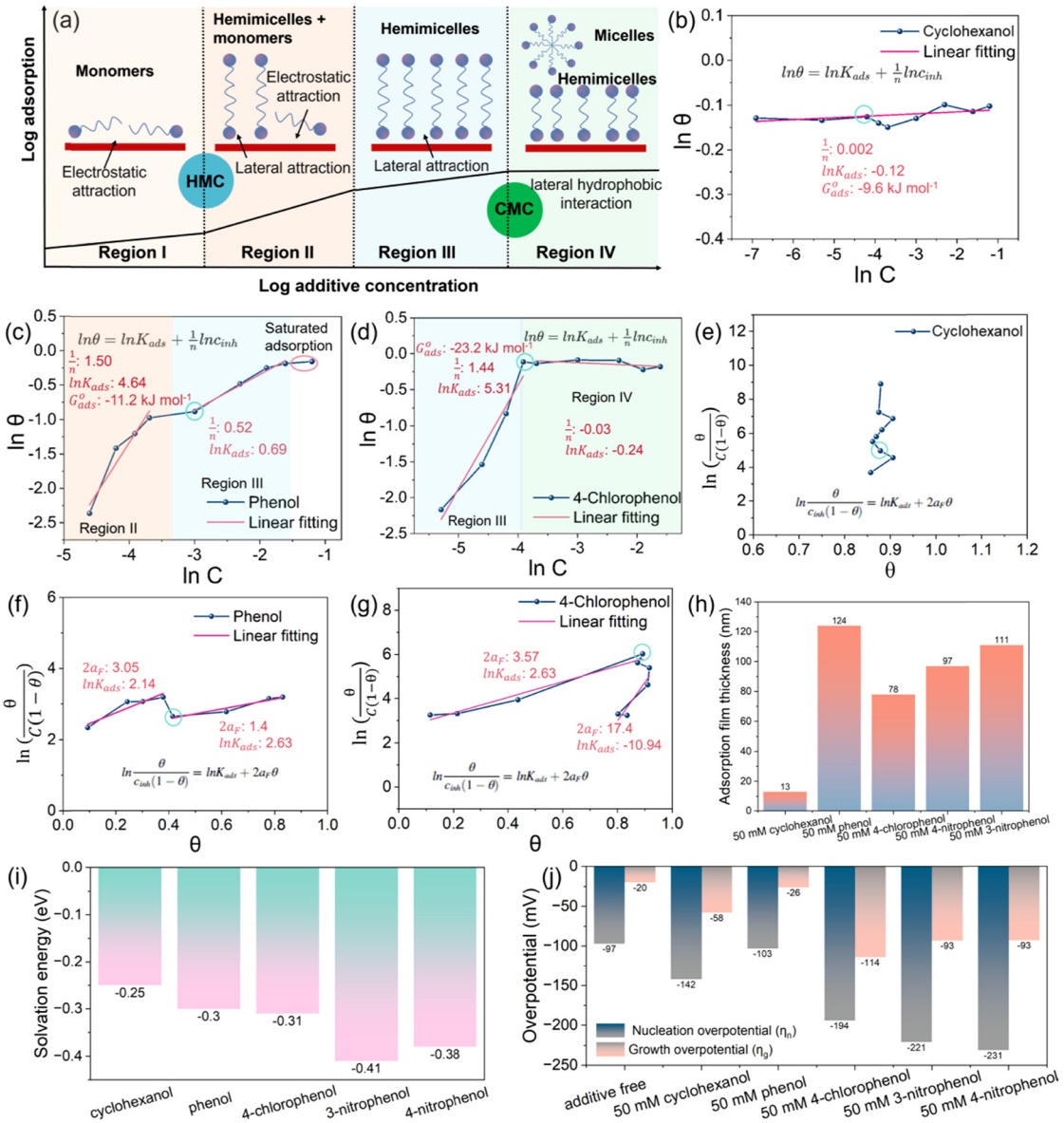


Fig. 2 Dynamics of the additive filming on zinc surface and its role in regulating the nucleation and growth overpotentials. (a) The scheme of Somasundaran–Fuerstenau isotherm to demonstrate the relationship between concentration and adsorbent configuration. Freundlich adsorption isotherms for (b) cyclohexanol, (c) phenol, and (d) 4-chlorophenol additive-containing 1 M $Na_2SO_4$ aqueous solution. The optimal additive concentration (50 mM, as determined for phenol) is indicated by a blue circle in the plots. Frumkin adsorption isotherms for (e) cyclohexanol, (f) phenol, and (g) 4-chlorophenol additive-containing 1 M $Na_2SO_4$ aqueous solution. In all isotherms, the optimal additive concentration (50 mM, as determined for phenol) is indicated by a blue circle. (h) The corresponding adsorption layer thickness derived from the QCM-D data using the Broadfit viscoelastic model across multiple harmonics. (i) Calculated solvation energies of the organic additives. (j) Nucleation and growth overpotentials extracted from galvanostatic voltage profiles after 5 cycles at a current density of 2 mA $cm^{-2}$ for different electrolytes.

the non-equivalent nature of additive adsorption (see detailed analysis in the SI), the adsorption data for cyclohexanol, phenol, and 4-chlorophenol were first analyzed based on Freundlich isotherms (Tables S4–S6 and Fig. 2b–d) by plotting the $\ln\theta$ as a function of $\ln C$. For cyclohexanol (Fig. 2b), the surface coverage remains nearly constant with increasing concentration, yielding a very small slope (0.002), indicative of weak monolayer adsorption (region I). In contrast, phenol (Fig. 2c) exhibits two distinct regimes: a steep slope of 1.5 at low concentrations (region II), reflecting strong electrostatic and lateral interactions, followed by a reduced slope of 0.52 at higher concentrations (region III), consistent with hemimicelle-like adsorption. The optimal phenol concentration ($\sim$50 mM, blue circle), where the zinc rechargeability peaks as revealed above, lies near the transition between these regimes. These findings suggest that, at the working concentration, phenol primarily adsorbs as hemimicelle-like aggregates rather than forming a simple monolayer. Since region III corresponds to surface charge neutralization, the proximity of the optimal concentration to this transition explains the strong dependence

of zinc cycling performance on the phenol additive concentration. Achieving sufficient surface coverage is essential for stabilizing deposition, whereas excessive adsorption intensifies lateral interactions, weakening the effect of the adsorbed layer and ultimately compromising cycling stability. For 4-chlorophenol (Fig. 2d), adsorption initially resembles hemimicelle formation (slope = 1.44), but levels off beyond 50 mM, indicating saturation and a transition to region IV.

Furthermore, knowing the adsorption constant $K_{ads}$, obtained from the intercept of the linear fitting of the isotherm, the Gibbs free energy of adsorption $\Delta G^{\circ}_{ads}$ can be calculated using

$$\Delta G^{\circ}_{ads} = -RT\ln\left(C_{H_2O} \times K_{ads}\right) = -RT\ln(55.56 \times K_{ads}) \quad (1)$$

Here, $C_{H_2O} \sim 55.56$ mol kg$^{-1}$ is the molal concentration of water in the electrolyte solution. The derived $\Delta G^{\circ}_{ads}$ values (Fig. 2b–d) exhibit a trend consistent with theoretical adsorption energies, reflecting increasing adsorption affinity in the order of cyclohexanol < phenol < 4-chlorophenol. It is important to note that, given the multi-regime nature of the adsorption isotherms for phenol and 4-chlorophenol, the $\Delta G^{\circ}_{ads}$ was calculated from the fitting of the region around the optimal concentration (50 mM). Cyclohexanol and phenol exhibit $\Delta G^{\circ}_{ads}$ values of −9.6 and −11.2 kJ mol$^{-1}$, respectively – both less negative than −20 kJ mol$^{-1}$ – consistent with physisorption.[31] In contrast, 4-chlorophenol exhibits a more negative value (−23.2 kJ mol$^{-1}$), indicating mixed physisorption–chemisorption behavior.

Beyond zinc–additive interactions, lateral forces between adsorbed molecules – governed by π–π and other van der Waals interactions – also play a critical role in determining interfacial adsorbate structure. These interactions can promote the formation of organized assemblies such as hemimicelles and micelles. To capture these effects, the Frumkin isotherm was applied, incorporating an interaction parameter ($\alpha_F$) that quantifies attractive or repulsive forces among adsorbed species (see the SI). As shown in Fig. 2e, the cyclohexanol isotherm exhibits an almost vertical profile, indicating a high $\alpha_F$ value and strong intermolecular interactions. These interactions restrict the degrees of freedom of additive molecules within the adsorption layer, weakening additive–metal binding,[32] particularly for species with low intrinsic surface affinity (as seen in the Freundlich model). This results in a dense but thin monolayer, which can be insufficient to effectively regulate Zn plating/stripping or suppress side reactions such as hydrogen evolution and Zn self-corrosion, ultimately contributing to zinc deposition instability and hence premature short-circuit failure. Similar to the Freundlich model, the Frumkin isotherms for phenol and 4-chlorophenol (Fig. 2f and g) display two linear regimes, reflecting concentration-dependent interfacial behavior. In the low $\theta$ region, both additives exhibit moderately positive interaction parameters ($\alpha_F$), indicating favorable intermolecular interactions. At higher surface coverage, phenol shows a reduced $\alpha_F$ (1.4), suggesting lower interfacial packing, while 4-chlorophenol exhibits a significantly higher $\alpha_F$ (17.4), indicative of strong lateral attraction and dense molecular packing. Around 50 mM concentration, 4-chlorophenol forms a denser adsorption layer than phenol; combined with its strong surface affinity, this can impede $Zn^{2+}$ transport and contribute to overpotential-induced short-circuiting (see below).

To further investigate the formation and reversibility of additive films at the metal–electrolyte interface, quartz crystal microbalance with dissipation monitoring (QCM-D) was employed. This technique enables real-time tracking of mass changes and viscoelastic properties of adsorbed layers on the sensor surface.[33] Full experimental details and analysis are provided in the SI (Fig. S6–S10). QCM-D measurements reveal that these additives form interfacial films with pronounced dissipation ($\Delta D > 1$ ppm) and nonlinear $\Delta f - \Delta D$ responses across harmonics, indicative of soft, viscoelastic, and dynamically evolving adsorption layers (see the SI for detailed analysis). The thickness of the adsorbed film was estimated by fitting frequency responses across harmonics using the Broadfit viscoelastic model (Fig. 2h). Aromatic additives form significantly thicker layers than cyclohexanol (13 nm), attributed to strong π–metal interactions and moderate intermolecular forces, consistent with isotherm predictions (see above). Interestingly, phenol derivatives – 4-nitrophenol (111 nm), 3-nitrophenol (97 nm), and 4-chlorophenol (78 nm) – exhibit thinner films despite more negative adsorption energies. This trend aligns with Frumkin isotherm analysis, where stronger intermolecular interactions lead to denser, thinner additive layers.

Solvation energy reflects the thermodynamic tug-of-war between an additive's preference to remain in the aqueous phase and its tendency to adsorb onto the metal surface. Molecules with highly negative solvation energies (Fig. 2i), such as phenol derivatives, are stabilized by hydrogen bonding with water, which can hinder their interfacial adsorption. In contrast, cyclohexanol, with a less negative solvation energy, is less stabilized in solution and thus more inclined to self-assemble at the interface. Phenol, with moderate solvation energy, strikes an optimal balance between aqueous affinity, adsorption on metal, and interfacial mobility. This balance facilitates the formation of a thicker, more dynamic adsorption layer, as supported by QCM-D measurements.

Although the phenol derivatives form adsorption layers of comparable thickness to phenol, they exhibit markedly different zinc rechargeability, underscoring the critical role of additive film properties. Electrochemical impedance spectroscopy (EIS) reveals that 4-chlorophenol, 3-nitrophenol, and 4-nitrophenol generate significantly higher charge transfer resistance (Fig. S11), consistent with their densely packed, strongly bound adsorption layers that hinder $Zn^{2+}$ transport at the zinc–electrolyte interface. In contrast, cyclohexanol's weakly adsorbed, thin film permits facile ion transfer but fails to stabilize Zn deposition or suppress side reactions. Phenol, however, strikes an effective balance: its moderate adsorption energy and self-organizing intermolecular interactions yield a thick, dynamic film that regulates $Zn^{2+}$ flux without imposing a substantial transport barrier, while also protecting against corrosion.

The overpotential observed during Zn deposition also offers valuable insight into the nature of the adsorption film. Zn nucleation must overcome three energy barriers – charge

transfer, surface energy, and diffusion – whose combined effects are reflected in the galvanostatic voltage profile.[34,35] While these contributions are difficult to isolate, distinct voltage regimes provide useful indicators. The nucleation overpotential ($\eta_n$) marks the onset of polarization and reflects charge transfer and surface energy barriers, while the subsequent voltage plateau, or growth overpotential ($\eta_g$), captures the influence of bulk mass transport and surface diffusion barriers (Fig. S12).[36] As shown in Fig. 2j, strongly adsorbing additives like 4-nitrophenol and 3-nitrophenol exhibit elevated $\eta_n$ and $\eta_g$, indicating that the strong additive–metal and intermolecular interactions at the interface foster the formation of a firmly bound dense additive layer, which impedes $Zn^{2+}$ transport and nucleation. 4-Chlorophenol, despite its only slightly higher adsorption energy than phenol and comparable ionic conductivities (mass transport) with other electrolytes (Fig. S13), shows an even higher $\eta_g$ (−114 mV), likely due to its particularly compact film structure, as also predicted by isotherm analysis, which significantly restricts the surface diffusion.[37] In contrast, phenol enables facile zinc nucleation and growth, with $\eta_n$ (−103 mV) and $\eta_g$ (−26 mV) closely matching those of the additive-free electrolyte, consistent with its dynamic, moderately adsorptive film that supports efficient ion transport observed *via* EIS (Fig. S11). Interestingly, cyclohexanol, despite forming a thinner film, exhibits higher overpotentials ($\eta_n$ = −142 mV, $\eta_g$ = −58 mV), likely due to its compact and rigid adsorption layer that restricts interfacial kinetics, but enhances corrosion (Fig. S14) might as well have a critical role to play. These observations reinforce that both the adsorption strength of the additive on zinc and the intermolecular interactions among additive molecules at the interface jointly govern the structure and properties of the adsorbed film, thereby influencing zinc deposition dynamics.

Given the critical role of the additive layer in governing zinc nucleation and growth, the morphology of cycled Zn electrodes was systematically examined using SEM after 10 plating cycles at 2 mA $cm^{-2}$ and 2 mAh $cm^{-2}$. In the additive-free electrolyte, the Zn surface exhibits irregular agglomerates (Fig. S15 and S16a), which can lead to short-circuit failure, especially with thinner separators. Cyclohexanol, despite forming a compact adsorption layer, fails to suppress HER-induced corrosion due to its thin film, resulting in a mixed morphology of flaky agglomerates and hexagonal platelets (Fig. S16b). In contrast, phenol – with slightly stronger adsorption and enhanced film thickness – effectively blocks the HER and stabilizes zinc deposition, yielding a dense, orderly morphology free of ZSH byproducts (Fig. S16c). 4-Chlorophenol produces a relatively smooth surface, though some rough features persist (Fig. S16d). For 3-nitrophenol and 4-nitrophenol, the high nucleation and growth overpotentials lead to disordered, sheet-like agglomerates (Fig. S16e and f). Importantly, Raman and NMR spectra (Fig. S17) show no peak shifts across electrolytes, confirming that the observed morphological differences arise from variations in adsorption film properties, not changes in the solvation structure.

Taken together, these results highlight that the electrochemical performance of the additives is governed not by adsorption strength alone, but by the interplay between adsorption energetics and lateral intermolecular interactions. These factors collectively dictate the thickness, packing density, and mobility of the adsorbed layer, which in turn control interfacial $Zn^{2+}$ transport, nucleation behavior, and corrosion suppression.

### Effectiveness of the phenol additive in zinc deposition and corrosion control

Building on these insights, phenol was selected for detailed investigation due to its demonstrated ability to enhance zinc rechargeability through the formation of a highly effective adsorption layer. To probe the zinc microstructure evolution leading up to the final morphology, the early stages of the zinc deposition were visualized using SEM for the additive-free *vis-à-vis* phenol-containing electrolyte. As shown in Fig. 3a, for the phenol additive containing electrolyte, zinc initially nucleates and grows into a thin sheet-like microstructure, which progressively stacks into dense, multilayered clusters by 0.3 mAh $cm^{-2}$. This uniform growth continues with increasing capacity (0.5–2 mAh $cm^{-2}$), yielding tightly packed Zn platelets across the electrode, an outcome of the additive's interfacial regulation. In contrast, the additive-free electrolyte (Fig. 3b) also begins with sheet-like nucleation, but the flakes are finer and grow chaotically. As the deposition proceeds, these structures merge irregularly and orient vertically, forming honeycomb-like clusters consistent with the disordered morphology observed after 10 cycles (Fig. S16a). These results suggest that phenol's adsorbed layer effectively suppresses lateral diffusion and irregular growth, promoting a uniform, layered Zn architecture. This was further corroborated by *in situ* optical microscopy (Fig. S17), which revealed dendrite-free deposition in the phenol electrolyte. Importantly, Raman and NMR spectra (Fig. S18) show no peak shifts across electrolytes, confirming that the observed morphological differences arise from variations in adsorption film properties, not changes in the $Zn^{2+}$ solvation structure. While phenol can be oxidized at a high potential, which could limit its compatibility with some high voltage cathodes, linear sweep voltammetry (LSV) analysis of phenol-containing electrolytes, as shown in Fig. S19, confirms that phenol oxidation initiates at ~2.16 V *vs.* $Zn^{2+}$/Zn. This lies well above the operating voltage range of typical AZIB cathodes, confirming its stability within the typical AZIB operational window. Nevertheless, X-ray photoelectron spectroscopy (XPS) analysis, as presented in Fig. S20, further affirms that phenol remains chemically stable during cycling, with no evidence of decomposition or SEI formation, reinforcing that the observed morphology control arises purely from its adsorption dynamics.

To further probe interfacial processes during Zn deposition, distribution of relaxation times (DRT) analysis was applied to *in situ* EIS data (Fig. S21) collected every 3 minutes during the progressive zinc deposition in the two electrolytes. DRT effectively deconvolutes overlapping electrochemical signals, revealing distinct kinetic features. Peaks in the 0.001–0.01 s range correspond to charge transfer resistance ($R_{ct}$), while those near $10^{-5}$ s indicate the buildup of SEI or insulating byproducts like ZSH ($R_{ZSH}$).[38,39] As evident from Fig. 3c, in the

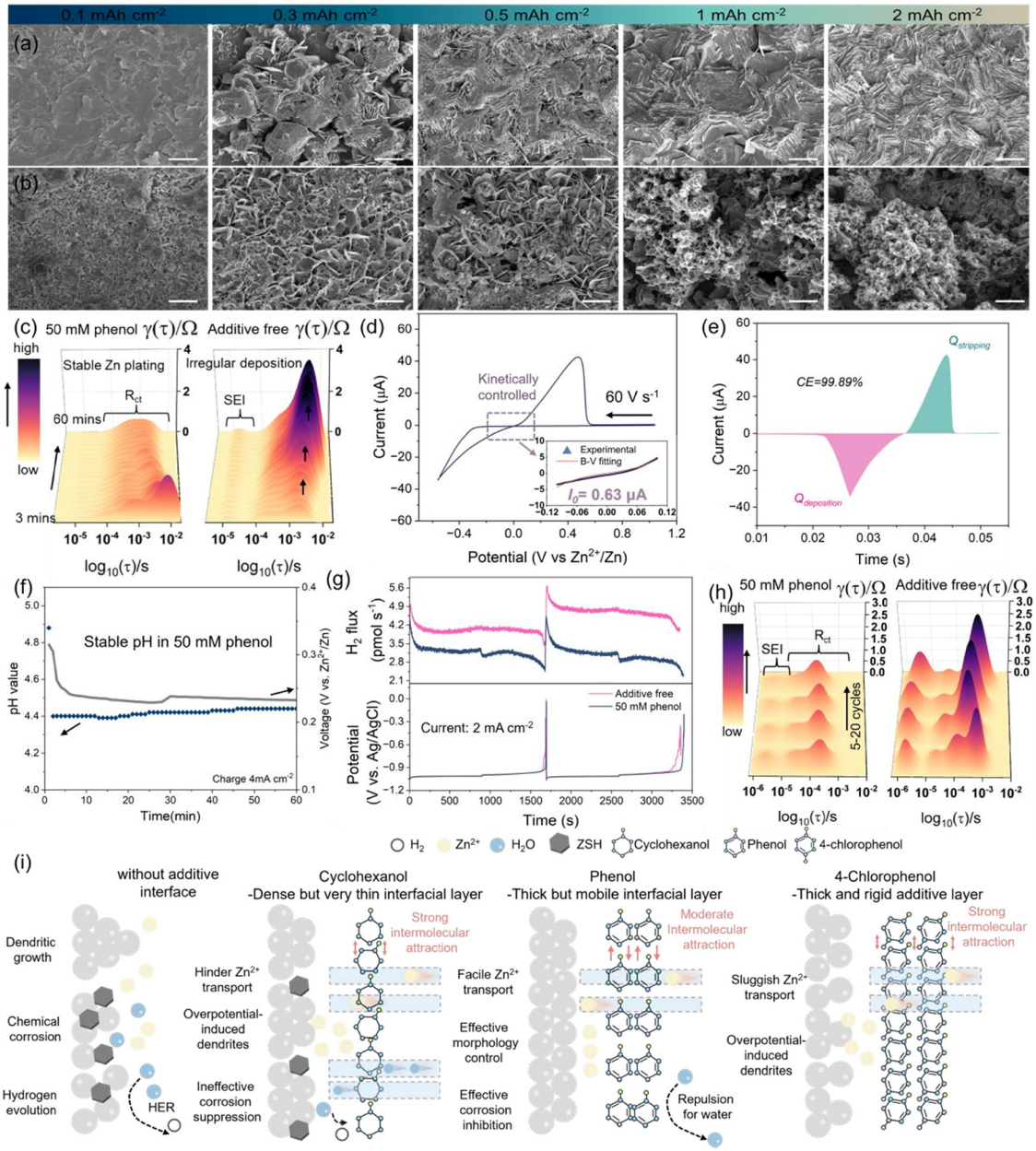


Fig. 3 The effect of the phenol additive on early-stage deposition control and corrosion inhibition. The evolution of the deposition microstructure during the early stages in (a) phenol containing and (b) baseline electrolytes at a current density of 2 mA cm$^{-2}$. (c) The DRT analysis of the *in situ* EIS data, revealing the corrosion dynamics in phenol-containing and baseline electrolytes during the first deposition. (d) Fast-scan cyclic voltammogram (60 V s$^{-1}$) recorded in 50 mM phenol electrolyte using a tungsten ultramicroelectrode as the working electrode and Ag/AgCl as the combined counter/reference electrode. (e) Corresponding current–time plot derived from (d), used to determine the CE of Zn electrodeposition. (f) *In situ* pH measurements for 50 mM phenol electrolytes, measured at 4 mA cm$^{-2}$. (g) *In situ* differential electrochemical mass spectrometry curves of Ti–Pt–Ag/AgCl cell cycling at a current of 2 mA cm$^{-2}$ in the additive-free and 50 mM phenol electrolytes with corresponding voltage profile. (h) The DRT analysis for the two electrolytes during long-term cycling (5–20 cycles). (i) Schematic diagrams illustrating the interfacial reaction pathways at the Zn anode under varying interfacial conditions: from no adsorption layer in a conventional electrolyte to thin, moderate, and thick adsorptive interphase.

phenol-containing electrolyte, $R_{ct}$ progressively stabilizes during cycling, and no $R_{ZSH}$ peak emerges – highlighting phenol's ability to maintain efficient charge transfer and suppress corrosion. In contrast, the additive-free electrolyte shows a growing $R_{ZSH}$ signal and rising $R_{ct}$, consistent with ZSH accumulation that impedes interfacial kinetics.

Intrinsic charge-transfer kinetics of zinc electrodeposition was investigated by employing an ultramicroelectrode (UME). Unlike conventional macroelectrodes, UMEs enable time-resolved measurements under well-defined kinetic control, minimizing mass-transfer limitations and capacitive distortions.[40] As shown in Fig. 3d, a well-defined kinetic region (±10% of

peak current) was accessed at 60 V $s^{-1}$ in 50 mM phenol electrolyte.[41] Fitting this region using the Butler–Volmer model yields an exchange current ($I_0$) of 0.63 μA, slightly lower than the baseline (1.08 μA, Fig. S22a), attributed to phenol–film formation and the associated overpotential increase discussed above. In addition to kinetic insights, UME study also allows precise CE evaluation by minimizing side reactions during the short scan window. Notably, the CE in phenol-containing electrolyte reached 99.89% (Fig. 3e), significantly higher than 95.94% in the baseline electrolyte (Fig. S22b), indicating improved reversibility. The stable deposition and effective corrosion suppression with the phenol-containing electrolyte is further supported by *in situ* pH measurements (Fig. 3f), where the interfacial pH remains stable at 4.4, indicating minimal HER activity. However, in the baseline electrolyte, the pH rises from 4.4 to 4.77 during the 60-minute deposition cycle (Fig. S23), suggesting HER-induced alkalization. The observed rise in pH, which likely reaches even higher at the electrode surface, will trigger ZSH formation, which, in turn, will push the charge transfer barrier and trigger deposition inhomogeneity. To accurately quantify gas production, *in situ* differential electrochemical mass spectrometry (DEMS, Fig. 3g) was conducted for the two electrolytes at 2 mA $cm^{-2}$, showing that 50 mM phenol markedly suppresses hydrogen evolution and sustains a lower $H_2$ flux with a more stable potential than that in additive-free electrolyte. This is attributed to the interaction between the phenol-derived adsorption film and water-solvated $Zn^{2+}$ ($Zn(H_2O)^2{}_6{}^+$), which, as supported by DFT (see Fig. S24), facilitates $Zn^{2+}$ desolvation by displacing coordinated water molecules. This process is likely driven by $Zn^{2+}$ interactions with the phenolic –OH group and π-electrons, while the hydrophobic nature of the aromatic π-framework likely further helps promote the stripping of solvated water molecules. Eventually, this leads to suppression of water-induced side reactions at the interface. DRT analysis of the EIS data during prolonged cycling (Fig. 3h and Fig. S25) reinforces the observation noted above: phenol maintains stable $R_{ct}$ with minimal SEI formation, while the baseline electrolyte shows progressive increase in charge transfer resistance due to continuous ZSH buildup. X-ray diffraction (XRD) analysis of the cycled zinc (Fig. S26) confirms the formation of ZSH in the baseline electrolyte, whereas phenol enables corrosion-free cycling without detectable byproduct formation.

Since the severity of the corrosion would be particularly obvious during cycling at high DoD, when the corrosion can quickly exhaust the finite Zn source, the corrosion-mediated zinc loss during cycling was quantified in the Zn–Ti cell (10 μm Zn). As shown in Fig. S27, capacity loss owing to corrosion after various cycles was evaluated by fully stripping Zn from electrodes with known initial mass. While some Zn loss is inevitable, the phenol-containing electrolyte significantly mitigates corrosion, retaining 83% of Zn capacity after 50 cycles compared to 73% for the additive-free electrolyte. As corrosion can spontaneously proceed even during rest, the effect of the phenol additive on corrosion inhibition during resting was further studied. After 24 hours of resting, SEM and EDS mapping (Fig. S28) reveal extensive ZSH byproduct coverage on Zn anodes in the baseline electrolyte. In contrast, for the phenol-containing electrolyte, electrodes remain smooth and planar without the proliferation of ZSH (Fig. S29 and S30). To summarize, the distinctive adsorption mechanism of the phenol additive is illustrated in Fig. 3i. Unlike cyclohexanol, which forms a dense yet thin adsorption layer that inadequately suppresses water-induced side reactions and restricts $Zn^{2+}$ transport due to tightly packed molecular arrangements, phenol presents a more favorable interfacial configuration. Its considerably high adsorption energy, coupled with moderate intermolecular interactions, leads to a loosely packed but adequately thick adsorption layer. This structure not only promotes rapid $Zn^{2+}$ transport and diffusion but also effectively mitigates parasitic reactions by shielding the Zn surface from water exposure. The thick phenol layer can also strip off the solvated water molecules from $Zn^{2+}$ and thereby suppress the HER. An interesting contrast is offered by 4-chlorophenol: despite exhibiting a comparable adsorption thickness and even stronger binding affinity to Zn than phenol, it forms an overly compact interfacial layer. This excessive molecular packing hampers $Zn^{2+}$ mobility, intensifies interfacial polarization, resulting in non-uniform Zn deposition.

To gain deeper insight into the impact of corrosion on Zn reversibility, the coulombic efficiency (CE) of Zn–Ti cells was tracked during cycling at 2 mA–2 mAh $cm^{-2}$, with a 24-hour pause after each plating step. As shown in Fig. S31, the 24-hour rest induces a noticeable drop in CE for the baseline electrolyte. Falling to 93.6% in the first cycle compared to 98.7% without resting, indicating significant chemical corrosion of plated Zn during the idle period. The CE continues to decline with cycling, reaching 92.3% by the 10th cycle. In sharp contrast, the phenol-containing electrolyte maintains a higher initial CE of 95.1%, which improves to 97.1% by the 10th cycle, providing unequivocal evidence of its excellent chemical (rest period will induce) and electrochemical corrosion mitigation.

### Phenol's effect on Zn anode rechargeability

Expanding upon the above findings, the effectiveness of phenol in extending zinc rechargeability was further evaluated under stringent conditions. Symmetric Zn–Zn cells were assembled using 20 μm Zn electrodes, a ~200 μm (soaked-pressed) glass fiber separator, and a limited electrolyte volume of 50 μL (12.5 μL $mAh^{-1}$). These cells were cycled at 4 mA $cm^{-2}$ and 4 mAh $cm^{-2}$ areal current and capacity conditions. As shown in Fig. 4a, the phenol-containing electrolyte enabled stable cycling for over 1000 hours (500 cycles), compared to just 290 hours in the baseline electrolyte. To more accurately assess Zn reversibility, without the influence of the zinc reserve present in symmetric cells,[10] the focus shifted to Zn–Ti asymmetric cells, which are more sensitive to short-circuiting and zinc depletion. All other cycling conditions were kept constant. As illustrated in Fig. 4b, when cycling at 2 mA $cm^{-2}$ and 2 mAh $cm^{-2}$ (corresponding to 17% Zn DoD of Zn), the phenol additive enables remarkably stable cycling for over 1000 hours, with a promising average coulombic efficiency (CE) of 99.4% (Fig. 4c), while the

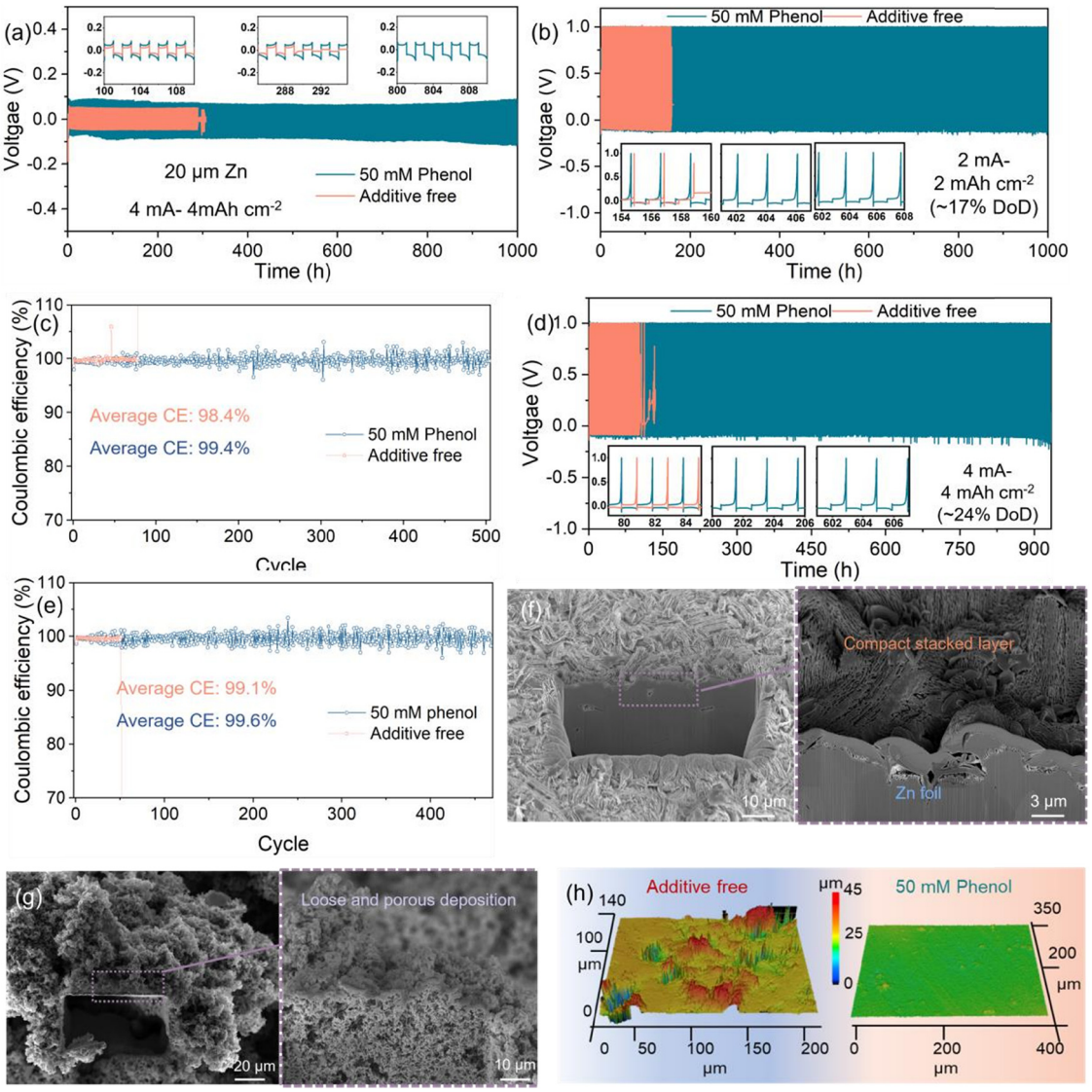


Fig. 4 Enhanced rechargeability of the Zn anode enabled by the phenol additive. (a) Voltage–time profiles for Zn cycling in additive-free and 50 mM phenol electrolyte at 4 mA $cm^{-2}$ and 4 mAh $cm^{-2}$ in Zn–Zn symmetric cells with 20 μm Zn. Galvanostatic voltage profile for Zn–Ti asymmetric cell cycled with additive-free baseline and 50 mM phenol electrolytes at (b) 2 mA $cm^{-2}$ and 2 mAh $cm^{-2}$ (20 μm Zn, 17%DoD) and (d) 4 mA $cm^{-2}$ and 4 mAh $cm^{-2}$ (30 μm Zn, 24%DoD), with the corresponding CE evolution during cycling shown in (c) and (e), respectively. The focused ion beam (FIB)-SEM images after cycling in (f) 50 mM phenol and (g) additive-free electrolyte. (h) Laser confocal scanning microscopy images of Zn electrodes after 10th plating in the two electrolytes.

baseline electrolyte and other additive-containing electrolytes (Fig. S32 and S33) suffers from premature short-circuit failure. The improved CE (99.6%, Fig. S34) in the phenol electrolyte was further confirmed by the Aurbach method. This enhanced performance under shallow cycling conditions reflects a relatively "Zn-rich" regime, where corrosion-induced polarization is effectively mitigated. However, in the absence of phenol, deposition instability persists, leading to dendritic growth that ultimately triggers failure. As anticipated, a relatively thick 30 μm zinc electrode – yet corresponding to a rather high 24% DoD – further extends the zinc anode lifespan in the phenol electrolyte to 930 hours even under 4 mA–4 mAh $cm^{-2}$ cycling, with a high CE of 99.6% (Fig. 4d and e). Notably, regardless of whether a symmetric or asymmetric configuration is employed, or whether cycling parameters such as areal capacity or electrode thickness are varied, the dominant factor governing performance remains the available zinc reserve. As previously discussed, the extent of corrosion scales with Zn utilization depth, leading to divergent failure modes in the baseline electrolyte. In contrast, the phenol additive consistently delivers superior rechargeability across all tested conditions, underscoring its versatility and the functional advantages of its thick and dynamic adsorption layer.

As cycling progresses, irregular zinc deposits in the additive-free electrolyte aggregate into coral-like dendrites, as revealed by cross-sectional SEM imaging (Fig. S35a). These dendritic

 

structures reach a thickness of ~160 μm, approaching the critical threshold for separator penetration and short-circuiting. In stark contrast, the Zn anode cycled in the phenol-containing electrolyte (Fig. S35b) exhibits a morphology closely resembling that of the pristine electrode (Fig. S36), with a flat and uniform surface. Notably, the deposited layer features a distinctive terraced architecture, characterized by wave-like contours and stacked ridges (inset in Fig. S35b). To further investigate the internal structure, focused-ion beam (FIB)-SEM analysis was conducted. As shown in Fig. 4f, the Zn electrode cycled in the phenol-containing electrolyte reveals a compact and stacked microstructure with high structural order and density. Conversely, the additive-free system (Fig. 4g) forms a sponge-like network of loosely aggregated deposits and voids, indicative of uncontrolled growth and poor mechanical integrity. This stark morphological contrast underscores the role of phenol in promoting layered, uniform zinc deposition – a key factor in its ability to endow superior cycling stability. Surface roughness analysis *via* laser confocal scanning microscopy (LCSM, Fig. 4h) further supports this observation. While the additive-free electrolyte yields a lumpy, heterogeneous surface, the phenol electrolyte results in a smooth, uniform topography, comparable to pristine zinc foil (Fig. S37). In summary, the exceptional long-term cycling performance enabled by phenol stems from its ability to foster dendrite-free, layered zinc growth. This is achieved through multifaceted regulation at the electrode–electrolyte interface, including modulation of charge transfer, surface diffusion, nucleation dynamics, and suppression of parasitic side reactions.

### Full-cell and pouch-cell performance validation

A representative Zn‖ZVO full cell was assembled using $Zn_{0.25}V_2O_5{\cdot}nH_2O$ (ZVO) as the cathode and Zn metal as the anode to assess whether the enhanced Zn rechargeability

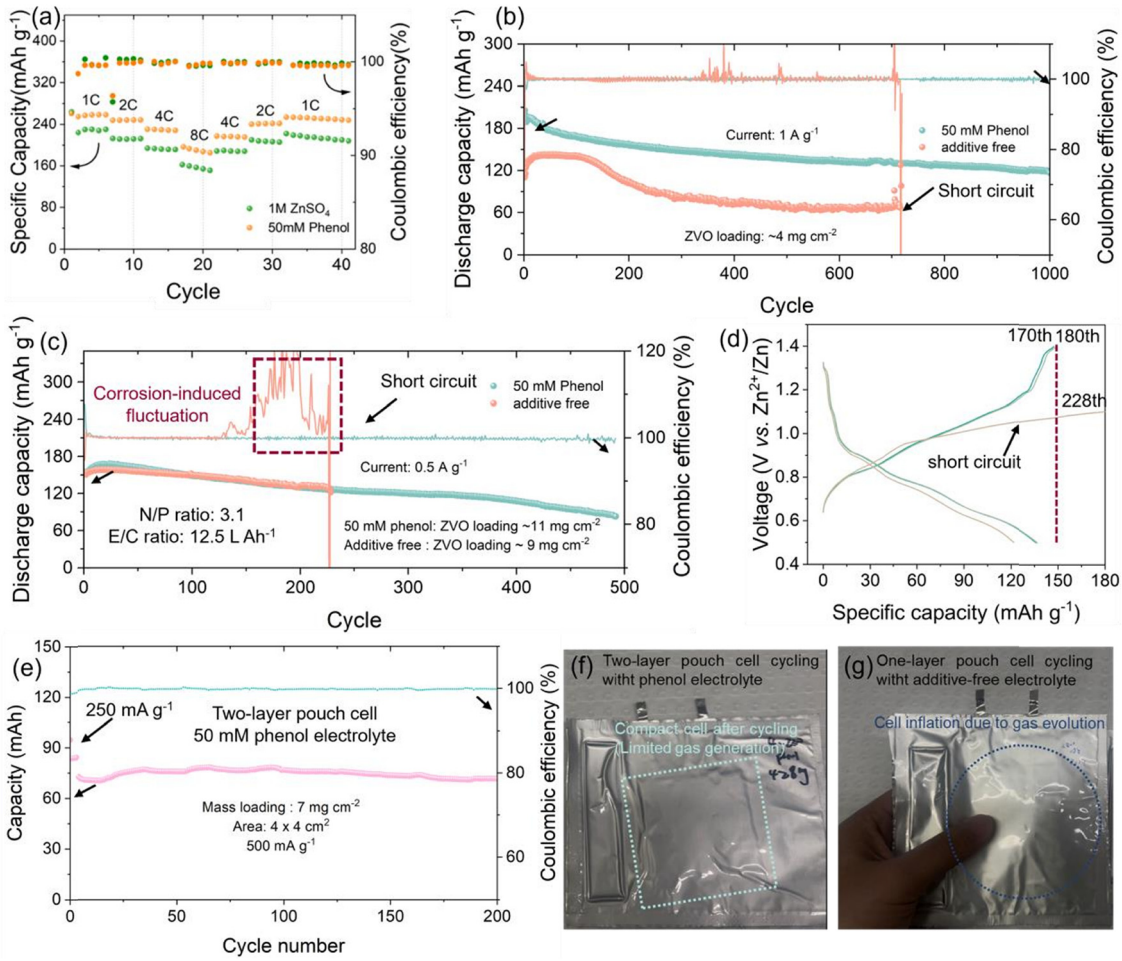


Fig. 5 Effect of the phenol additive on the Zn‖ZVO full-cell performance. (a) Rate capability testing with the phenol-containing and baseline electrolytes. (b) The long-term cycling test of ZVO‖Zn cells (ZVO loading ~ 4 mg $cm^{-2}$) with the two electrolytes at 1 A $g^{-1}$ current density. (c) Cycling performance of the ZVO‖Zn cells for an N/P ratio = 3.1, tested with an ultra-thin Zn anode and high ZVO loading, at a current density of 0.5 A $g^{-1}$ and (d) the corresponding voltage–capacity profiles for the additive-free electrolyte showing the short circuit failure induced by zinc dendrite formation. (e) The corresponding cycling performance of ZVO‖Zn pouch cell (4 cm × 4 cm, two-layer cell with double-coated ZVO electrode) with 428 mg total ZVO loading, cycling in 50 mM phenol electrolyte at 0.5 A $g^{-1}$. The digital picture of the ZVO‖Zn pouch cell after 200 cycles with (f) 50 mM phenol electrolyte and (g) additive-free electrolyte to demonstrate the gas evolution and corresponding cell swelling issue in the absence of the phenol additive.

observed in the phenol-containing electrolyte translates to full-cell performance. The ZVO was synthesized *via* a standard hydrothermal method, with its nanofiber morphology and layered crystal structure confirmed by SEM and XRD (Fig. S38 and S39). As shown in Fig. 5a, the phenol electrolyte delivers excellent rate capability, achieving specific capacities of 258, 248, 230, and 190 mAh $g^{-1}$ at 1, 2, 4, and 8C (1C = 250 mAh $g^{-1}$), respectively, within a narrow voltage window (0.5–1.4 V). In comparison, the baseline electrolyte yields lower capacities of 230, 212, 192, and 157 mAh $g^{-1}$ under identical conditions and active mass loading. Long-term cycling results (Fig. 5b) for the Zn‖ZVO cell with a high Zn reserve (100 μm) and moderate ZVO loading (4 mg $cm^{-2}$) show that the optimized electrolyte retains ~60% of its capacity after 1000 cycles at 1 A $g^{-1}$, with an outstanding average CE of 99.94%. In contrast, the baseline electrolyte starts with a much lower initial capacity (110 mAh $g^{-1}$ *vs.* 200 mAh $g^{-1}$) and exhibits rapid capacity fading, retaining only 80 mAh $g^{-1}$ after 300 cycles, along with pronounced CE fluctuations. Both the continuous capacity degradation and unstable charge/discharge behavior point to the aggressive corrosion and ZSH precipitation on the anode side, thereby causing an increase in the overall cell impedance.

The effect of the phenol additive on full-cell performance was further validated under more stringent cycling conditions, involving a high active mass loading (11 mg $cm^{-2}$) and an ultrathin Zn anode (10 μm), yielding a low N/P ratio of ~3. As shown in Fig. 5c, under these deep cycling conditions, the full cell with the baseline electrolyte suffers from rapid short circuit failure at 224 cycles (Fig. 5d), consistent with the half-cell results discussed earlier. Notably, prior to failure, the cell exhibits pronounced CE fluctuations, attributed to intensified side reactions under high Zn utilization, which continuously convert active Zn into insulating ZSH at the anode. At such utilization levels, CE or voltage fluctuations caused by byproducts often coincide with short-circuit events. Therefore, corrosion – whether directly or indirectly influencing Zn deposition and promoting dendrite-induced short circuits – emerges as a more critical issue than often recognized and must be addressed alongside short-circuit mitigation.

While the Zn‖ZVO cell in the phenol electrolyte shows a similar initial capacity (158 mAh $g^{1}$) to that in the baseline, the additive significantly improves cyclability, maintaining a stable charge/discharge profile (Fig. S40) without CE fluctuations or short-circuiting for 500 cycles. To assess scalability, a two-layer Zn‖ZVO pouch cell was fabricated by coating ZVO on both sides of a stainless-steel foil (16 $cm^2$ × 2) and pairing it with a thin Zn anode (Fig. S41). The cell delivered an initial capacity of 71 mAh, before stabilizing around 78 mAh (182 mAh $g^{-1}$, Fig. 5e) at 0.5 A $g^{-1}$ and maintaining excellent stability over 200 cycles without any signs of cell swelling or gas evolution (Fig. 5f). In contrast, a single-layer pouch cell assembled with the same ZVO electrode, and the additive-free electrolyte exhibited 38 mAh roughly half the capacity of the two-layer cell, which is expected (Fig. S42). This cell showed a sharp decline in coulombic efficiency and increasing capacity mismatch between charge and discharge after 150 cycles, primarily due to gas evolution (Fig. 5g), which disrupts electrode–electrolyte contact and accelerates cell failure.

## Conclusions

Using phenol and its derivatives as model electrolyte additives, this work presents a systematic investigation into the role of adsorption dynamics in regulating zinc anode behavior in AZIBs. Among the tested candidates, phenol consistently outperforms both cycloaliphatic and more strongly adsorbing aromatic analogues in extending zinc anode rechargeability across all tested configurations. It enables over 1000 hours of stable cycling in symmetric cells and over 900 hours in asymmetric cells at 24% depth of discharge at 4 mA–4 mAh $cm^{-2}$ with a limited 12.5 μL $mAh^{-1}$ electrolyte to capacity ratio, with high coulombic efficiencies. Full-cell and pouch-cell tests further validate its practical viability, demonstrating stable operation under high loading, low N/P ratios, and extended cycling without gas evolution or short-circuit failure. Mechanistically, phenol achieves a unique balance between moderate adsorption strength and interfacial mobility, forming a thick yet dynamic film that facilitates $Zn^{2+}$ transport while suppressing HER-mediated corrosion, thus rendering effective morphological regulation and enhanced zinc reversibility over prolonged cycling. In contrast, additives with stronger binding energies form overly compact and thick but rigid interfacial additive layers that block ion transport and promote polarization-induced deposition instability. The weakly adsorbing cycloaliphatic additive furnishes a compact but thin additive layer, which proves ineffective in suppressing corrosion while deterring $Zn^{2+}$ transport, leading to only a slight improvement in rechargeability.

These findings challenge the prevailing notion that stronger adsorption is inherently better and instead highlight the importance of dynamic interfacial behavior. By decoupling the roles of additive adsorption energetics and spatial organization, packing density, and thickness of the additive film, this study reveals the mechanistic underpinnings dictating additive efficacy. The concept of tuning interfacial dynamics, rather than merely maximizing surface affinity, offers a new paradigm for electrolyte additive engineering and rationalizing their performance for enhanced zinc metal anode rechargeability.

## Author contributions

Yuan Shang: conceptualization, methodology, investigation, data curation, formal analysis, validation, and writing – original draft; Ravindra Kokate: methodology, investigation, and writing – original draft; Yingna Ding: methodology and investigation; Ashutosh Rana, Jeffrey E. Dick, Xinyuan Wu, Bram Hoex, Mingyue Wang, and Nana Wang: investigation and formal analysis; Qihui Zhang: methodology and investigation; Priyank Kumar: methodology, supervision, writing – review and editing, and funding acquisition; and Dipan Kundu: conceptualization, methodology, resources, data analysis, validation,

writing – original draft and review and editing, and funding acquisition.

## Conflicts of interest

A provisional patent application is being filed based on the findings reported in this work.

## Data availability

The data supporting the findings of this study are available within the article and its supplementary information (SI) file. Supplementary information is available. See DOI: **https://doi.org/10.1039/d5ee05206h**.

Additional raw data are available from the corresponding author upon reasonable request.

## Acknowledgements

D. K. and P. K. acknowledge the Australian Government – Dept. of Education's support through the AEA seed grant, and RACE2030 CRC funding. We also acknowledge the Mark Wainwright Analytical Center at UNSW for access and support with the characterization work presented here.

## References

1 X. Li, T. Zhang, G. Li, B. Wang, H. Jin, Y. Zhang, X. Liu, Y. Feng, Y. Wang, W. Zhou, J. Zhao, W. Li, H. Fan, D. Zhao and D. Chao, A Mn2+–S Redox Electrochemistry for Energetic Aqueous Manganese Ion Battery, *Joule*, 2025, **9**(6), 101930, DOI: **10.1016/j.joule.2025.101930**.

2 D. Chao, W. Zhou, F. Xie, C. Ye, H. Li, M. Jaroniec and S.-Z. Qiao, Roadmap for Advanced Aqueous Batteries: From Design of Materials to Applications, *Sci. Adv.*, 2020, **6**, eaba4098, DOI: **10.1016/j.joule.2025.101930**.

3 P. Ruan, S. Liang, B. Lu, H. J. Fan and J. Zhou, Design Strategies for High-Energy-Density Aqueous Zinc Batteries, *Angew. Chem., Int. Ed.*, 2022, **134**(17), e202200598, DOI: **10.1002/ange.202200598**.

4 Y. Shang and D. Kundu, Understanding and Performance of the Zinc Anode Cycling in Aqueous Zinc-Ion Batteries and a Roadmap for the Future, *Batteries Supercaps*, 2022, **5**(5), e202100394, DOI: **10.1002/batt.202100394**.

5 Q. Yang, Q. Li, Z. Liu, D. Wang, Y. Guo, X. Li, Y. Tang, H. Li, B. Dong and C. Zhi, Dendrites in Zn-Based Batteries, *Adv. Mater.*, 2020, **32**(48), 2001854, DOI: **10.1002/adma.202001854**.

6 X. Yu, Z. Li, X. Wu, H. Zhang, Q. Zhao, H. Liang, H. Wang, D. Chao, F. Wang, Y. Qiao, H. Zhou and S.-G. Sun, Ten Concerns of Zn Metal Anode for Rechargeable Aqueous Zinc Batteries, *Joule*, 2023, **7**(6), 1145–1175, DOI: **10.1016/j.joule.2023.05.004**.

7 K. Zhou, Z. Li, X. Qiu, Z. Yu and Y. Wang, Boosting Zn Anode Utilization by Trace Iodine Ions in Organic-Water Hybrid Electrolytes through Formation of Anion-Rich Adsorbing Layers, *Angew. Chem., Int. Ed.*, 2023, **62**(39), e202309594, DOI: **10.1002/anie.202309594**.

8 C. Li, X. Xie, S. Liang and J. Zhou, Issues and Future Perspective on Zinc Metal Anode for Rechargeable Aqueous Zinc-Ion Batteries, *Energy Environ. Mater.*, 2020, **3**(2), 146–159, DOI: **10.1002/eem2.12067**.

9 J. Hao, X. Li, X. Zeng, D. Li, J. Mao and Z. Guo, Deeply Understanding the Zn Anode Behaviour and Corresponding Improvement Strategies in Different Aqueous Zn-Based Batteries, *Energy Environ. Sci.*, 2020, **13**(11), 3917–3949, DOI: **10.1039/D0EE02162H**.

10 Y. Shang, Z. Tong and D. Kundu, Decoding the Zinc Depletion-Mediated Failure in Aqueous Zinc Batteries: On Limiting Parameters and Accurate Assessment, *ACS Energy Lett.*, 2024, **9**(6), 3084–3092, DOI: **10.1021/acsenergylett.4c00967**.

11 Z. Wu, Y. Wang and C. Zhi, Zinc-Anode Reversibility and Capacity Inflection as an Evaluation Criterion, *Joule*, 2024, **8**(9), 2442–2448, DOI: **10.1016/j.joule.2024.07.023**.

12 S. Liu, J. Mao, W. K. Pang, J. Vongsvivut, X. Zeng, L. Thomsen, Y. Wang, J. Liu, D. Li and Z. Guo, Tuning the Electrolyte Solvation Structure to Suppress Cathode Dissolution, Water Reactivity, and Zn Dendrite Growth in Zinc-Ion Batteries, *Adv. Funct. Mater.*, 2021, **31**(38), 2104281, DOI: **10.1002/adfm.202104281**.

13 M. Shi, C. Lei, H. Wang, P. Jiang, C. Xu, W. Yang, X. He and X. Liang, Molecule Engineering of Sugar Derivatives as Electrolyte Additives for Deep-Reversible Zn Metal Anode, *Angew. Chem., Int. Ed.*, 2024, **136**(35), e202407261, DOI: **10.1002/ange.202407261**.

14 B. Zhang, J. Yao, C. Wu, Y. Li, J. Liu, J. Wang, T. Xiao, T. Zhang, D. Cai, J. Wu, Z. W. Seh, S. Xi, H. Wang, W. Sun, H. Wan and H. J. Fan, Electrolyte Design for Reversible Zinc Metal Chemistry, *Nat. Commun.*, 2025, **16**(1), 71, DOI: **10.1038/s41467-024-55657-1**.

15 F. Wang, O. Borodin, T. Gao, X. Fan, W. Sun, F. Han, A. Faraone, J. A. Dura, K. Xu and C. Wang, Highly Reversible Zinc Metal Anode for Aqueous Batteries, *Nat. Mater.*, 2018, **17**, 543–549, DOI: **10.1038/s41563-018-0063-z**.

16 L. Cao, D. Li, T. Pollard, T. Deng, B. Zhang, C. Yang, L. Chen, J. Vatamanu, E. Hu, M. J. Hourwitz, L. Ma, M. Ding, Q. Li, S. Hou, K. Gaskell, J. T. Fourkas, X. Q. Yang, K. Xu, O. Borodin and C. Wang, Fluorinated Interphase Enables Reversible Aqueous Zinc Battery Chemistries, *Nat. Nanotechnol.*, 2021, **16**, 902–910, DOI: **10.1038/s41565-021-00905-4**.

17 K. Fu, H. Wang, M. Xie, Y. Zhang, Y. Xin, X. Xu, Y. Wu, Z. Li, Y. Luo, Y. Ma, C. Liu, D. Ma, H. Huang, Y. Liao, F. Zeng and X. Liang, Self-Assembly of Super-Hydrophobic and Zincophilic Surface Monolayer for Durable Zn Anodes, *Energy Storage Mater.*, 2025, **78**, 104281, DOI: **10.1016/j.ensm.2025.104281**.

18 L. Ma, T. P. Pollard, M. A. Schroeder, C. Luo, Y. Zhang, G. Pastel, L. Cao, J. Zhang, V. Shipitsyn, Y. Yao, C. Wang, O. Borodin and K. Xu, Engineering a Zinc Anode Interphasial

Chemistry for Acidic, Alkaline and Non-Aqueous Electrolytes, *Energy Environ. Sci.*, 2024, **17**(7), 2468–2479, DOI: **10.1039/D4EE00062E**.

19 Y. Lv, C. Huang, M. Zhao, M. Fang, Q. Dong, W. Tang, J. Yang, X. Zhu, X. Qiao, H. Zheng, C. Sun, L. Zheng, M. Zheng, Y. Xu and J. Lu, Synergistic Anion–Cation Chemistry Enables Highly Stable Zn Metal Anodes, *J. Am. Chem. Soc.*, 2025, **147**(10), 8523–8533, DOI: **10.1021/jacs.4c16932**.

20 H. Li, J. Hao and S.-Z. Qiao, AI-Driven Electrolyte Additive Selection to Boost Aqueous Zn-Ion Batteries Stability, *Adv. Mater.*, 2024, **36**(49), 2411991, DOI: **10.1002/adma.202411991**.

21 R. Chen, Y. Zhong, P. Jiang, H. Tang, F. Guo, Y. Dai, J. Chen, J. Wang, J. Liu, S. Wei, W. Zhang, W. Zong, F. Zhao, J. Zhang, Z. Guo, X. Wang and G. He, Untangling the Role of Capping Agents in Manipulating Electrochemical Behaviors Toward Practical Aqueous Zinc-Ion Batteries, *Adv. Mater.*, 2025, 2412790, DOI: **10.1002/adma.202412790**early view.

22 F. Wu, J. Zhang, L. Ma, P. Ruan, Y. Chen, S. Meng, R. Yin, W. Shi, W. Liu, J. Zhou and X. Cao, Directing Zn Growth with Biased Adsorption of Straight-Chain Molecules for Superior Zn Anode Stability, *Angew. Chem., Int. Ed.*, 2025, **64**(11), e202421787, DOI: **10.1002/anie.202421787**.

23 Y. Shang, V. Kundi, I. Pal, H. N. Kim, H. Zhong, P. Kumar and D. Kundu, Highly Potent and Low-Volume Concentration Additives for Durable Aqueous Zinc Batteries: Machine Learning-Enabled Performance Rationalization, *Adv. Mater.*, 2024, **36**(9), 2309212, DOI: **10.1002/adma.202309212**.

24 J. Kumankuma-Sarpong, C. Chang, J. Hao, T. Li, X. Deng, C. Han and B. Li, Entanglement Added to Cross-Linked Chains Enables Tough Gelatin-Based Hydrogel for Zn Metal Batteries, *Adv. Mater.*, 2024, **36**(30), 2403214, DOI: **10.1002/adma.202403214**.

25 Z. Zheng, X. Zhong, Q. Zhang, M. Zhang, L. Dai, X. Xiao, J. Xu, M. Jiao, B. Wang, H. Li, Y. Jia, R. Mao and G. Zhou, An Extended Substrate Screening Strategy Enabling a Low Lattice Mismatch for Highly Reversible Zinc Anodes, *Nat. Commun.*, 2024, **15**(1), 753, DOI: **10.1038/s41467-024-44893-0**.

26 H. Li, Y. Li, M. Liu, Z. Yang, Y. Gong, J. Qian, R. Zhang, Y. Bai, F. Wu and C. Wu, Biocrust-Inspired Interface Layer with Dual Functions towards Highly Reversible Zinc Metal Anodes, *Energy Environ. Sci.*, 2025, **18**(6), 2973–2984, DOI: **10.1039/D4EE06048B**.

27 Z. Li, Z. Wang, W. Sun, Y. Ma, W. Guo and Y. Fu, Regulating Interface Engineering by Helmholtz Plane Reconstructed Achieves Highly Reversible Zinc Metal Anodes, *Adv. Mater.*, 2025, **37**(14), 2420489, DOI: **10.1002/adma.202420489**.

28 S. Li, Y. Zhong, J. Huang, G. Lai, L. Li, L. Jiang, X. Xu, B. Lu, Y. Liu and J. Zhou, Regulating Interfacial Kinetics Boosts the Durable A H-Level Zinc-Ion Batteries, *Energy Environ. Sci.*, 2025, **18**(5), 2599–2609, DOI: **10.1039/D4EE04372C**.

29 K. Wang, H. Zhan, W. Su, X. Liu and X. Sun, Ordered interface regulation at Zn electrodes induced by trace gum additives for high-performance aqueous batteries, *Energy Environ. Sci.*, 2025, **18**(3), 1398–1407, DOI: **10.1039/D4EE04100C**.

30 H. Ma, H. Chen, M. Chen, A. Li, X. Han, D. Ma, P. Zhang and J. Chen, Biomimetic and Biodegradable Separator with High Modulus and Large Ionic Conductivity Enables Dendrite-Free Zinc-Ion Batteries, *Nat. Commun.*, 2025, **16**(1), 1014, DOI: **10.1038/s41467-025-56325-8**.

31 D. Wang, L. Gao, D. Zhang, D. Yang, H. Wang and T. Lin, Experimental and Theoretical Investigation on Corrosion Inhibition of AA5052 Aluminium Alloy by L-Cysteine in Alkaline Solution, *Mater. Chem. Phys.*, 2016, **169**, 142–151, DOI: **10.1016/j.matchemphys.2015.11.041**.

32 C. G. Vaszilcsin, M. V. Putz, A. Kellenberger and M. L. Dan, On the Evaluation of Metal-Corrosion Inhibitor Interactions by Adsorption Isotherms, *J. Mol. Struct.*, 2023, **1286**, 135643, DOI: **10.1016/j.molstruc.2023.135643**.

33 P. T. McNamara and C. F. Blanford, A Sensitivity Metric and Software to Guide the Analysis of Soft Films Measured by a Quartz Crystal Microbalance, *Analyst*, 2016, **141**(10), 2911–2919, DOI: **10.1039/C6AN00143B**.

34 J. L. Barton and J. O. 'M. Bockris, The Electrolytic Growth of Dendrites from Ionic Solutions, *Proc. R. Soc. London, Ser. A*, 1962, **268**, 485–505, DOI: **10.1098/rspa.1962.0154**.

35 A. Pei, G. Zheng, F. Shi, Y. Li and Y. Cui, Nanoscale Nucleation and Growth of Electrodeposited Lithium Metal, *Nano Lett.*, 2017, **17**, 1132–1139, DOI: **10.1021/acs.nanolett.6b04755**.

36 P. Biswal, S. Stalin, A. Kludze, S. Choudhury and L. A. Archer, Nucleation and Early Stage Growth of Li Electrodeposits, *Nano Lett.*, 2019, **19**, 8191–8200, DOI: **10.1021/acs.nanolett.9b03548**.

37 M. Kim, J. Lee, Y. Kim, Y. Park, H. Kim and J. W. Choi, Surface Overpotential as a Key Metric for the Discharge–Charge Reversibility of Aqueous Zinc-Ion Batteries, *J. Am. Chem. Soc.*, 2023, **145**(29), 15776–15787, DOI: **10.1021/jacs.3c01614**.

38 Y. Dai, C. Zhang, W. Zhang, L. Cui, C. Ye, X. Hong, J. Li, R. Chen, W. Zong, X. Gao, J. Zhu, P. Jiang, Q. An, D. J. L. Brett, I. P. Parkin, G. He and L. Mai, Reversible Zn Metal Anodes Enabled by Trace Amounts of Underpotential Deposition Initiators, *Angew. Chem., Int. Ed.*, 2023, **62**(18), e202301192, DOI: **10.1002/anie.202301192**.

39 L. Yao, J. Liu, F. Zhang, B. Wen, X. Chi and Y. Liu, Reconstruction of Zinc-Metal Battery Solvation Structures Operating from −50 ∼ +100 °C, *Nat. Commun*, 2024, **15**(1), 6249, DOI: **10.1038/s41467-024-50219-x**.

40 A. Rana, Md. A. Faisal, K. Roy, J. H. Nguyen, S. Paul and J. E. Dick, How the Kinetic Balance Between Charge-Transfer and Mass-Transfer Influences Zinc Anode Stability: An Ultramicroelectrode Study, *Small Methods*, 2025, **9**(3), 2401021, DOI: **10.1002/smtd.202401021**.

41 A. J. Bard, L. R. Faulkner and H. S. White, *Electrochemical Methods: Fundamentals and Applications*, 3rd edn, Wiley-VCH Verlag GmbH, Weinheim, 2022.